JOURNAL OF CHEMICAL INFORMATION AND MODELING

Article

pubs.acs.org/jcim

Structural Insight into the Unique Binding Properties of Pyridylethanol(phenylethyl)amine Inhibitor in Human CYP51

Urška Zelenko,[†] Milan Hodošček,[‡] Damjana Rozman,[§] and Simona Golič Grdadolnik*[,†,∥]

[†]Laboratory of Biomolecular Structure, National Institute of Chemistry, Hajdrihova 19, 1001 Ljubljana, Slovenia

[‡]Laboratory of Molecular Modeling, National Institute of Chemistry, Hajdrihova 19, 1001 Ljubljana, Slovenia

[§]Center for Functional Genomics and Bio-Chips, Faculty of Medicine, University of Ljubljana, 1000 Ljubljana, Slovenia

[∥]EN-FIST Centre of Excellence, Dunajska 156, 1000 Ljubljana, Slovenia

Supporting Information

ABSTRACT: Sterol 14α-demethylase (CYP51) is the main drug target for the treatment of fungal infections. The discovery of new efficient fungal CYP51 inhibitors requires an understanding of the structural requirements for selectivity for the fungal over the human ortholog. In this study, a binding mode of the pyridylethanol-(phenylethyl)amine type CYP51 inhibitor to the human ortholog was determined at the atomic level. We isolated and purified a full-length human CYP51. The inhibitor-specific binding and its conformational and dynamic properties were evaluated using UV−visible and NMR spectroscopy. Considering the experimental data in docking calculations and molecular dynamics simulations, the location of the inhibitor moieties and their interactions with the enzyme active site were determined. The inhibitor binds to the enzyme in two diastereomeric forms, which have a common location of aromatic ring moieties, while the less bulky propyl chain can adapt to various hydrophobic regions of the enzyme active site. The halogenated phenyl ring binds in the substrate access channel making numerous contacts with the hydrophobic side chains, and its interactions with the unconserved residues are especially informative. The results reveal the unique binding properties of the investigated inhibitor in comparison to the azoles and provide novel directions for the design of selective fungal inhibitors.

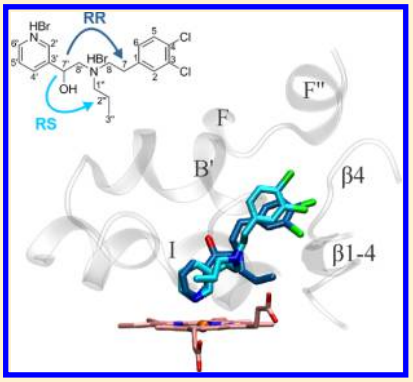

1. INTRODUCTION

Sterol 14α-demethylase (CYP51) catalyzes a key step in the sterol biosynthetic pathway, the oxidative removal of the 14α-methyl group from sterol precursors. The enzyme belongs to a superfamily of cytochromes P450 (CYPs) and is the only CYP found in all biological kingdoms.[1] Contrary to drug metabolizing CYPs, CYP51 has a very narrow substrate specificity, limited to five naturally occurring 14α-methylsterols.[1] The final products of the sterol biosynthetic pathway are cholesterol in animals, ergosterol in fungi, and phytosterols in plants. These sterols are essential structural components of eukaryotic membranes, regulating their fluidity and permeability, and thus, they are essential for the survival of many organisms. Due to its key role in the biosynthesis of ergosterol, CYP51 is the main drug target for the treatment of human infections with fungi.

Azoles are broadly known CYP51 inhibitors and are currently the most widely used antifungals in clinical medicine and agriculture.[2] The mode of action of the azoles is coordination to the heme iron with basic nitrogen in the protein active site, thus preventing substrate binding and metabolism. Accumulation of toxic 14α-methylsterols and the depletion of membrane-associated ergosterol change the cell membrane properties and lead to the inhibition of fungal cell growth.[3] The basis for azole efficacy is their selective inhibition of fungal CYP51 over the human ortholog. However, prolonged and prophylactic use of azoles can inhibit other human CYP enzymes and lead to drug resistance.[3] Also, the incidence of opportunistic fungal infections has increased worldwide as a consequence of the rising number of immunocompromised individuals. Despite available antifungal drugs, the mortality rate due to invasive fungal infections remains high and often exceeds 50%.[4] Therefore, new, more selective, and efficient inhibitors of fungal CYP51 are needed. The structural requirements for selectivity are not yet understood, most probably because of the lack of information from high-resolution ligand−CYP51 structures. So far, three crystal structures of CYP51 inhibitors with fungal and human CYP51 orthologs are available in the Protein Data Bank (PDB).

It was only recently that the first complete crystal structure of eukaryotic wild-type CYP51 from *Saccharomyces cerevisiae* was solved.[5] This is the first crystal structure of a fungal CYP51 and the only complete structure of a bitopic membrane protein deposited in the PDB. Other crystal structures of eukaryotic CYP51s were determined for N-truncated enzymes without the transmembrane helix: from protozoan pathogens, *Trypanosoma brucei*,[6,7] *Trypanosoma cruzi*,[7,8] *Leishmania infantum*[9], and from

Received: September 12, 2014
Published: November 24, 2014

   dx.doi.org/10.1021/ci500556k | *J. Chem. Inf. Model.* 2014, 54, 3384−3395

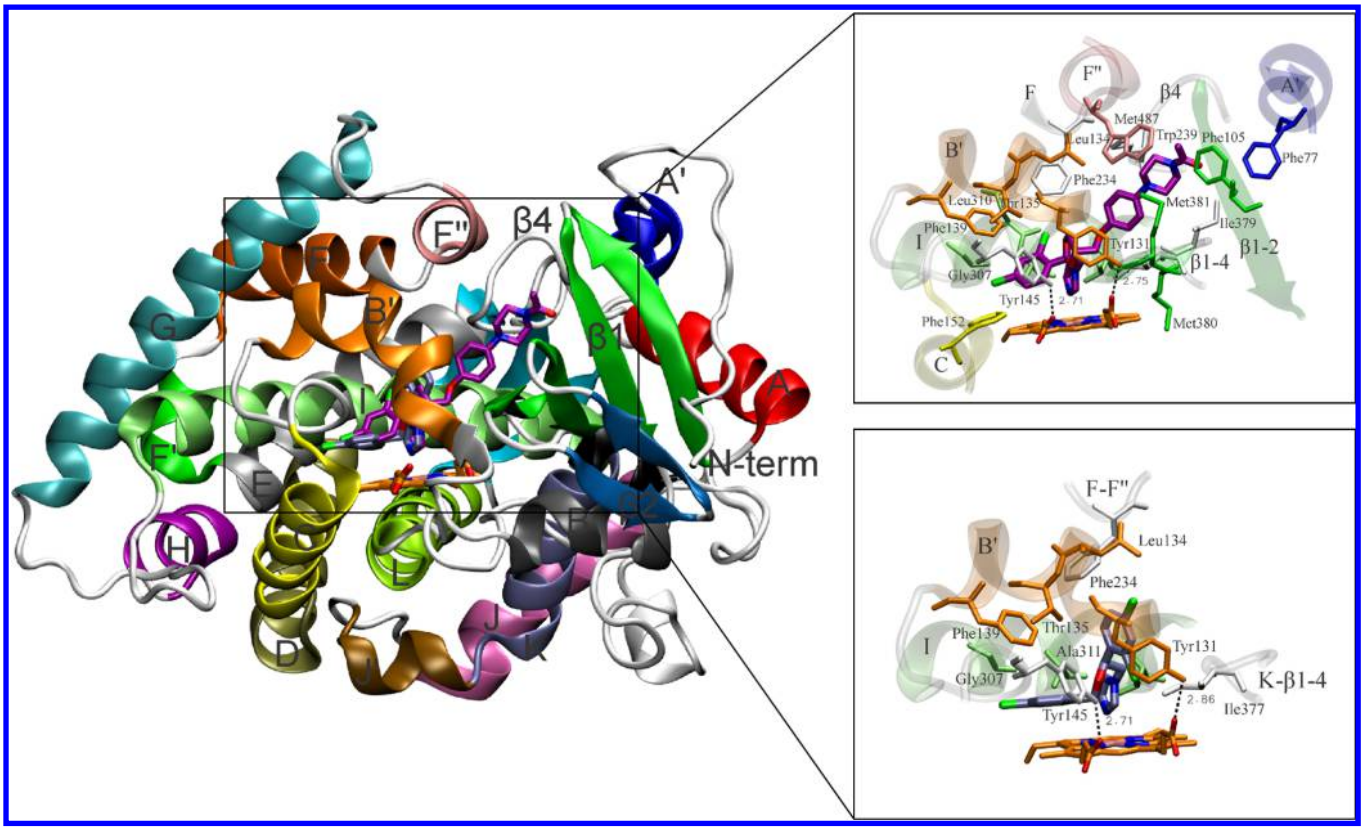

Figure 1. (Left) Overall structure of N-truncated hCYP51 in complex with ketoconazole (purple, PDB entry 3LD6) and superimposed econazole (ice blue, PDB entry 3JUS).[10] Secondary structure elements are presented in different colors and labeled. The heme is shown in orange. On the right is the hCYP51 active site with bound ketoconazole and econazole. The amino acids within 4 Å of each ligand are shown and colored in different colors that correspond to the color of the secondary structure element. The oxygen, nitrogen, and chlorine atoms are in red, blue, and green, respectively. The distances between the heme propionates and the side chain oxygens of Tyr131 and Tyr145 are given.

human.[10] There is no crystal structure of CYP51 from any pathogenic fungi. Although the primary sequence identity of CYP51 across biological kingdoms is low, their three-dimensional structure is highly similar and has a typical P450 fold,[11] which consists mainly of α-helices (Figure 1). In the eukaryotic CYP51, the heme is buried inside the protein and is surrounded by two nearly parallel helices, I and L. The entrance into the substrate access channel is formed by helices A′ and F″ and the β4 loop on the upper side of the protein. This portion of the protein is embedded into the endoplasmic reticulum membrane, and the sterol substrates enter the active site through the membrane.[5] The active site cavity is bordered by the heme, B′ helix−B′−C loop, N-terminal parts of helices C and I, β1−4 strand with the preceding K-β1−4 loop, and the β4 loop (Figure 1). The most characteristic feature of the eukaryotic CYP51 structure is the rigidity of the substrate binding cavity, which together with a highly similar general fold, probably helps to maintain their strictly specific three-step catalytic reaction.[12]

The superposition of seven *T. cruzi* and seven *T. brucei* CYP51 drug-target complexes showed that inhibitors branch into a Y-shape with an elongated "stem" and two shorter "arms".[13] The shortest arm orients toward the heme, with the aromatic nitrogen atom coordinating to the heme iron, whereas the longer arm extends into a hydrophobic channel near pyrrole ring D of the heme, presumably occupied by the aliphatic side chain of the sterol substrate. The elongated stem extends into the substrate access channel. While there are more than 15 available cocrystal structures of protozoan CYP51 in complex with different inhibitors, there are only two cocrystal structures of human CYP51 (hCYP51) in complex with ketoconazole and econazole (PDB entries 3LD6 and 3JUS)[10] (Figure 1) and one cocrystal structure of fungal CYP51 in complex with itraconazole (PDB entry 4K0F).[5] The azoles in human and *S. cerevisiae* CYP51 also branch into the Y-shape mentioned above. The aromatic nitrogen atom is coordinated to the heme iron. In ketoconazole and itraconazole, the longer arm, the dihalogenated phenyl ring extends into the hydrophobic channel near pyrrole ring D of the heme, and the elongated tail extends into the substrate access channel. The monohalogenated phenyl ring of econazole also extends into the hydrophobic channel near pyrrole ring D of the heme, but the conformation is nearly parallel with the heme plane. The dihalogenated phenyl ring of econazole is oriented toward the substrate access channel.

The determination of the binding mode of CYP51 inhibitors with novel structure scaffolds to the human ortholog is an important step for the development of inhibitors and for understanding the structural requirements for selectivity, which will enable the design of novel selective fungal CYP51 inhibitors. Therefore, we investigated the binding of a salt of 2-{[2-(3,4-dichloro-phenyl)-ethyl]-propyl-amino}-1-pyridin-3-yl-ethanol (**A**) (Figure 2) to hCYP51. This pyridylethanol-(phenylethyl)amine derivative caused a notable inhibition of cholesterol biosynthesis in a cell assay and was identified in follow-up studies as a specific inhibitor of CYP51, which coordinates to the heme iron through the pyridine nitrogen in an analogy with the azoles.[14,15] Extensive NMR studies of

dx.doi.org/10.1021/ci500556k | J. Chem. Inf. Model. 2014, 54, 3384−3395

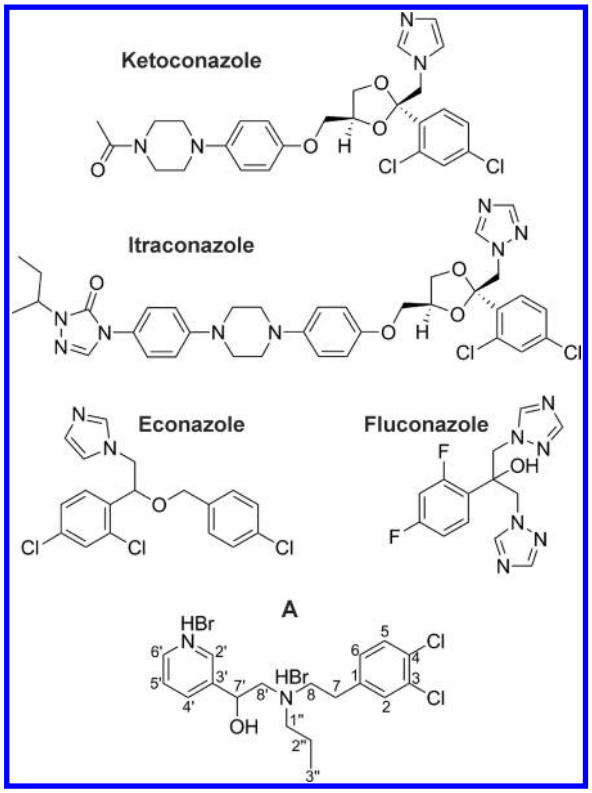

Figure 2. Structure of a salt of 2-{[2-(3,4-dichloro-phenyl)-ethyl]-propyl-amino}-1-pyridin-3-yl-ethanol (**A**) illustrating the atom nomenclature and structures of some azole inhibitors that are in clinical use and whose crystal structures with CYP51 orthologs have been solved.

compound **A**, free in a solution, were performed to explain its unusual NMR spectral properties.[16] A dynamic process causing a diastereomeric effect in the salt form of a racemic arylalkylamine structure was identified, and different conformational properties of a diastereomeric pair of compound **A** were revealed. Due to the dynamic nature of compound **A**, our studies of ligand binding to hCYP51 are based on the solution NMR and molecular dynamics (MD) simulations. These two techniques allow the exploration of dynamic processes in ligand−receptor complexes, which cannot be identified in rigid crystal structures but can affect ligand binding and biological activity.

Here, we report the results of combined experimental (UV−visible and NMR spectroscopy) and theoretical (docking, MD simulations, and Bennett's acceptance ratio (BAR) method) studies of conformation, dynamics, and interactions of compound **A** in the hCYP51 binding site. For the experimental studies, the full-length hCYP51 was isolated and purified from *Escherichia coli*. The binding affinity of compound **A** was determined by spectrophotometric titration to the protein, which also verified its specific action. The ligand-based NMR methods, saturation transfer difference, and transferred NOE were used to investigate the properties of the bound ligand. The possible binding modes of compound **A**, as obtained by docking studies, were selected according to the observed NOE connectivities, explored with restrained and unrestrained MD simulations, and analyzed in relation to the azoles. The results reveal a unique spatial arrangement of the ligand moieties in the hCYP51 binding site, different from that observed in the azoles, and provide novel guidelines for the design of selective fungal CYP51 inhibitors.

2. RESULTS AND DISCUSSION

2.1. UV−Visible Spectroscopic Studies of Binding of Compound A to hCYP51: Specific Ligand Binding. The specific binding of compound **A** to the full-length hCYP51 was evaluated by spectral titration to the purified protein. Apparent dissociation constants were determined by nonlinear regression in GraphPad Prism version 5.04 for Windows (GraphPad Software, San Diego, CA, U.S.A.) by fitting the data to the rearrangement of the Morrison equation.[17] In the ligand-free state, the heme in CYP51 is hexacoordinated, with a water molecule bound to the iron as the sixth ligand. The binding of a basic nitrogen atom of azole, pyridine, or pyrimidine heterocyclic compounds to the heme iron replaces the water molecule from the sixth position[18] and causes a red shift in the Soret band maximum from 417 to 422−427 nm, which is known as a type II spectral response. These ligand-induced changes can be used to estimate the binding affinities of the ligands to CYP51.[19] The binding of compound **A** to hCYP51 caused a type II spectral response, with a peak at 429 nm and a trough at 409 nm (Figure 3). The Soret maximum in the

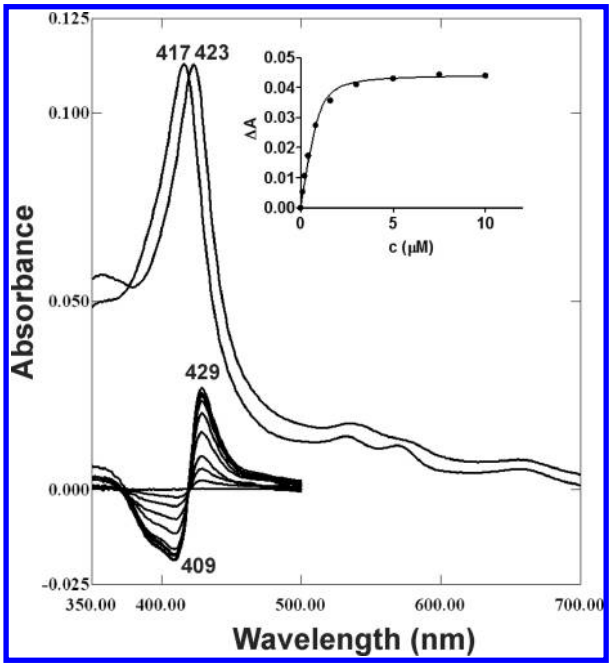

Figure 3. Spectral response of hCYP51 to compound **A**. Absolute (upper) and difference (lower) spectra and saturation curve of the absorbance change against compound **A** concentration ($\Delta A = \Delta A_{429-409}$) (right inset). The data were fit using a rearrangement of the Morrison equation.

absolute spectrum of the resultant compound **A**−hCYP51 complex shifted from 417 to 423 nm. This was caused by the coordination of the pyridine nitrogen to the sixth position of the heme iron.[15] Compound **A** bound tightly to the protein with a K_D value of 0.13 ± 0.03 μM. As a comparison, we used an azole inhibitor ketoconazole, which is coordinated to the heme iron through the imidazole ring N-3 nitrogen, also producing a type II spectral response. Ketoconazole bound very tightly to hCYP51, and the K_D value was estimated to be less than 0.050 μM.

dx.doi.org/10.1021/ci500556k | J. Chem. Inf. Model. 2014, 54, 3384−3395

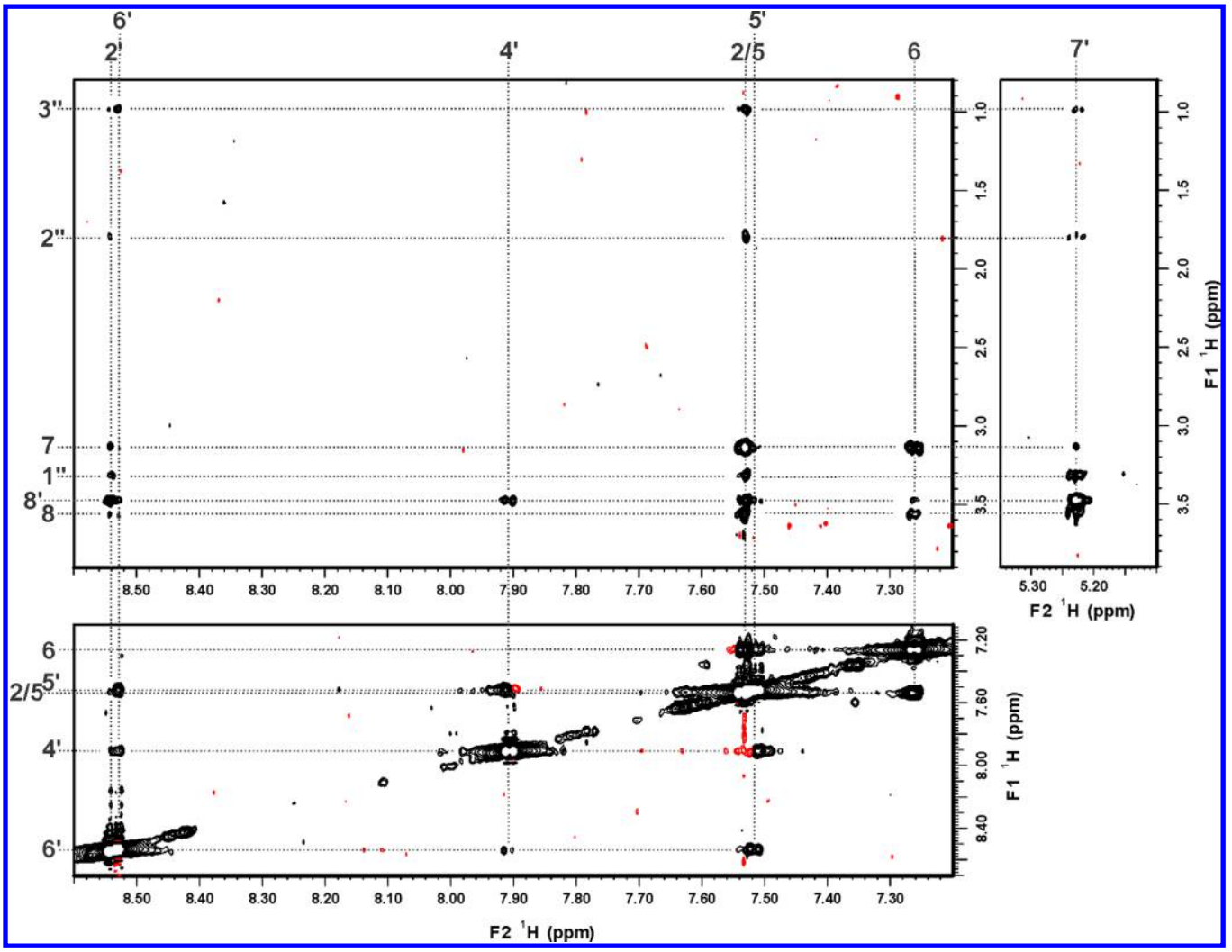

Figure 4. Expanded regions of the transferred NOESY spectrum of compound **A** in the presence of hCYP51 with the assignment of NOE connectivities. Weak NOE connectivities are clearly observed in the 1D traces. The signals of the H2 and H5 protons are largely overlapped. The line shapes of strong trivial NOE connectivities between the J-coupled H4′ and H5′ protons and between the J-coupled H5 and H6 protons are a little distorted because of the incomplete suppression of the zero quantum artifacts, and therefore, their maxima are slightly shifted.

2.2. NMR Spectroscopic Studies of Binding of Compound A to hCYP51: Bound Ligand Conformation and Ligand–Enzyme Contacts. The conformational and dynamic properties of compound **A** had been previously investigated in a solution by the application of NMR methods.[16] A dynamic process, which is causing an interesting case of a diastereomeric effect in this compound, was identified, and its mechanism was explained. The entire exchange process between diastereomers consists of acid dissociation, nitrogen inversion, nitrogen reprotonation, and conformational reorganization. In methanol at lower temperatures, the conformational analysis of each diastereomer could be performed. NOE connectivities indicated a different spatial arrangement of the ethanol, propyl, and ethyl chains in diastereomers, which was confirmed with molecular orbital calculations. Diastereomers have a different steric position of the H7′ proton relative to the propyl and ethyl chains. Only the RS diastereomer has the NOE connectivity between the H7′ proton and the H2″ protons in the propyl chain, while only the RR diastereomer has the NOE connectivity between the H7′ proton and the H7 protons in the ethyl chain. Therefore, these two mutually exclusive NOE connectivities can be used to identify the existence of both diastereomers in other media as well, where line broadening prevents the observation of a separate set of signals of a diastereomeric pair.

In this study, we investigated the conformational and dynamic properties of compound **A** in the hCYP51 binding site using the transferred NOESY experiment.[20,21] In the presence of the enzyme, a typical line broadening of ligand resonances was observed in the NMR spectra due to the exchange of a ligand between the free and bound form, hindering the observation of possible signal splitting due to inherent ligand flexibility. However, the presence of NOE cross-peaks between protons H7′ and H7 and between protons H7′ and H2″ in the transferred NOESY spectrum (Figure 4) indicates that compound **A** exists in both diastereomeric forms in the bound state as well. Contrary to the free ligand state, the NOE cross-peaks are observed between the propyl chain and the pyridine ring, as well as between the propyl chain and the dichlorophenyl ring. This is the only difference in the NOE pattern between the free and bound ligand states, which indicates a different relative orientation of the propyl chain with respect to the rings in the two ligand states. Probably in the bound form the flexibility of the propyl chain is also reduced.

dx.doi.org/10.1021/ci500556k | J. Chem. Inf. Model. 2014, 54, 3384−3395

Importantly, no NOE cross-peaks are observed between the rings, indicating that these two ligand moieties are located in remote parts of the enzyme active site.

The relative strength of interactions between the ligand and the enzyme were investigated with saturation transfer difference (STD) NMR[22,23] performed under quantitative conditions considering the nonuniform relaxation properties of compound **A**. The inversion recovery T_1 experiments showed that the ^1H T_1 relaxation times of compound **A** ranged from 0.7 s in the aliphatic part to 2.7 s in the aromatic part. Therefore, STD amplification factors were determined with a short saturation delay of 300 ms to avoid the effect of the longitudinal relaxation rate on the signal intensities.[24] The obtained STD ligand epitope map of compound **A** in the presence of hCYP51 (Figure 5) demonstrates that all the ligand moieties are in

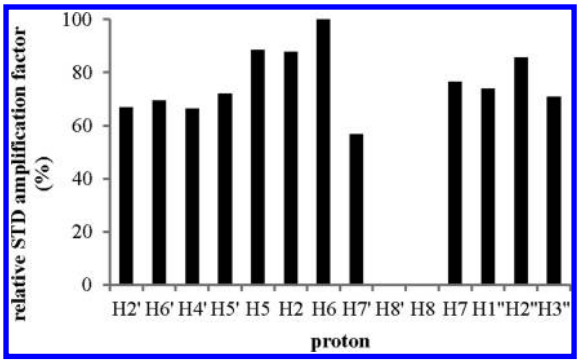

Figure 5. Relative degrees of saturation of individual protons of compound **A** determined from the STD NMR spectrum. The values are normalized to the intensity of the signal with the largest STD effect. The signals of the H8′ and H8 protons are overlapped with a buffer signal.

contact with the protein. The dichlorophenyl ring has a slightly stronger STD effect compared to the propyl chain and the pyridine ring.

The experimental studies of the binding of compound **A** to hCYP51 showed the following: (i) The ligand is coordinated to the heme iron through the pyridine nitrogen. (ii) All the ligand moieties are in contact with the protein, and the dichlorophenyl ring has slightly stronger interactions with the enzyme than the rest of the molecule. (iii) The ligand binds to the enzyme active site in two diastereomeric forms. (iv) In the bound ligand conformations, the propyl chain is in close spatial proximity to the dichlorophenyl and (or) pyridine ring, while the two rings are located in the remote parts of the binding site.

2.3. Molecular Modeling Studies of Binding of Compound A to hCYP51: Ligand Binding Mode. The possible binding poses of each diastereomer of compound **A** in the active site of hCYP51 were generated by molecular docking calculations using the Glide software (Glide, version 5.7, Schrödinger, LCC, New York, NY, 2011).[25−27] The binding poses with the low values of the GlideScore scoring function present the crucial differences in the locations of the ligand moieties (Figure 6). In each diastereomer, different locations of the dichlorophenyl ring and propyl chain are observed. The dichlorophenyl ring is located either in the hydrophobic channel near the pyrrole ring D of the heme (Figure 6A and C) or in the substrate access channel (Figure 6B and D). For the propyl chain, four representative locations are observed: (i) in the hydrophobic region bordered by the I helix and F−F″ loop (Figure 6A), (ii) in the hydrophobic channel near pyrrole ring D of the heme (Figure 6B), (iii) in the hydrophobic region bordered by the B′ helix and F−F″ loop, toward the substrate access channel (Figure 6C), and (iv) in the hydrophobic region bordered by the β1−4 strand (Figure 6D). Binding poses with the dichlorophenyl ring located in the hydrophobic channel near pyrrole ring D of the heme (Figure 6A and C) had the lowest value of the GlideScore scoring function.

Initially, these two binding poses were inspected. According to the binding mode of the azoles, these seemed to be the most probable binding poses. The halogenated phenyl ring is the only moiety of compound **A** that is also found in the azoles (Figure 2), and in all the available crystal structures of the azoles in complexes with CYP51 orthologs, the halogenated phenyl ring is located in this hydrophobic channel.[5,7−10] However, in such a position of the halogenated phenyl ring, its protons are in close spatial proximity to the protons of the pyridine ring in the case of compound **A** (<4 Å) or to the protons of the imidazole ring in the case of the azoles (<3.5 Å for ketoconazole, <3.5 Å for econazole) and should generate clear NOE connectivities in the transferred NOESY spectra. The absence of these NOE connectivities in the transferred NOESY spectrum (Figure 4) of compound **A** indicates that its dichlorophenyl ring is not positioned in the hydrophobic channel near pyrrole ring D of the heme. Nevertheless, the MD simulations for these two binding poses of compound **A** were performed to explore possible dynamic effects that may hinder observation of the NOE connectivities between the rings. The results showed that the overall location of the dichlorophenyl ring is stable in the binding site, and it is in close spatial proximity to the pyridine ring during the entire MD simulations (Figures S2 and S3, Supporting Information). Therefore, we excluded such binding poses as probable for compound **A** and further investigated only the binding poses that satisfy the remote position of the aromatic rings.

That is, the two representative binding poses with the dichlorophenyl ring positioned in the substrate access channel, which have the propyl chain located in either the hydrophobic channel near pyrrole ring D of the heme (Figure 6B) or in the hydrophobic region bordered by the β1−4 strand (Figure 6D), were investigated using NOE-restrained (3 ns) and unrestrained MD simulations (20 ns) at the receptor level for each diastereomer of compound **A**. Due to the dynamic nature of the free ligand and the possible conformational flexibility of the bound ligand, which can generate averaging of NOE connectivities between the two diastereomers or between different bound conformers, the distance constraints were carefully utilized. Only the upper bound distance limits, which can lead to observable NOE connectivity, and a minimum number of constraints that allowed the exploration of possible orientations of the propyl chain with respect to the aromatic rings were used. In every restrained MD simulation, a unique distance constraint of the H7′ proton either with the H2″ protons in the case of the RS diastereomer or with the H7 protons in the case of the RR diastereomer was applied. Violations of these distances were not observed in any MD simulation. Among the NOE connectivities between the protons of the propyl chain and the aromatic rings, only the strongest one of the propyl chain methyl group were selected as constraints, which are with the H2 (dichlorophenyl ring) and H6′ (pyridine ring) protons. These two restraints were applied either simultaneously or exclusively.

The application of restraints in the MD simulation changed the position of the propyl chain from the hydrophobic channel

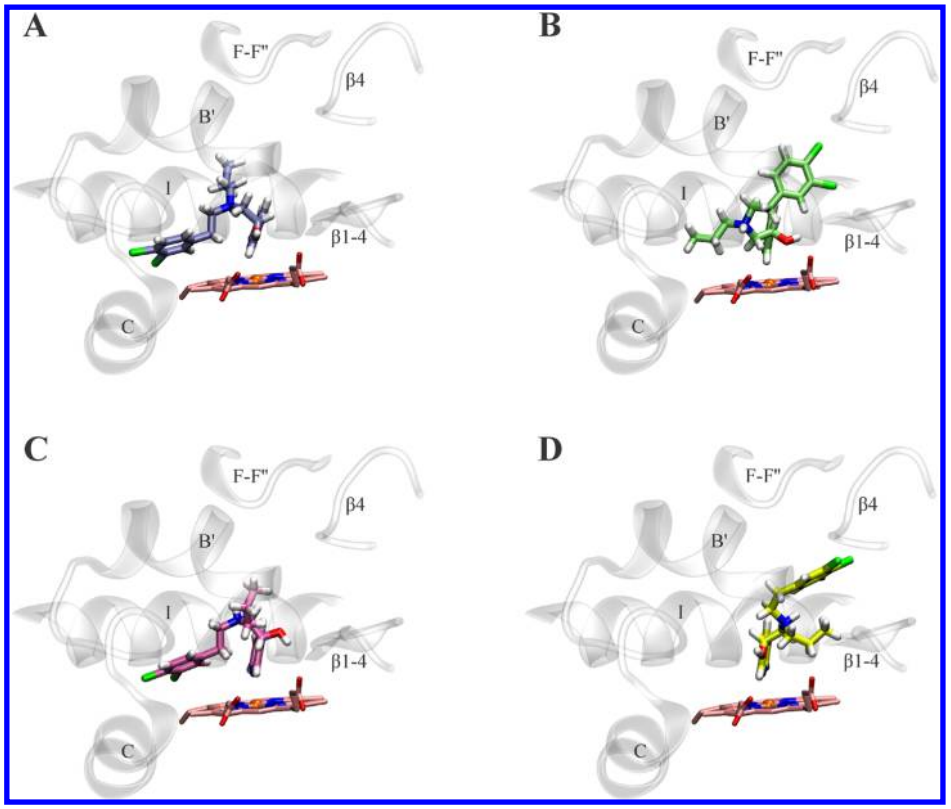

Figure 6. Representative binding poses of compound **A** in the active site of hCYP51 as obtained by molecular docking calculations: (A) and (B) RS diastereomer, (C) and (D) RR diastereomer. The images were generated in VMD.

near the pyrrole ring D of the heme (Figure 6B) to the nearby hydrophobic region bordered by helices I and B′ and the F−F″ loop. The overall location of the propyl chain then remained unchanged for both diastereomers in unrestrained MD simulations (Figure 7A and B). In the RS diastereomer, the propyl chain was oriented closer to the pyridine ring during the restrained and unrestrained MD simulations (Figure 7A and Figure S4, Supporting Information). In the RR diastereomer, the propyl chain was oriented away from both rings during the restrained and unrestrained MD simulations (Figure 7B and Figure S5, Supporting Information).

In MD simulations that started with the propyl chain initially positioned in the hydrophobic region bordered by the β1−4 strand (Figure 6D), the overall location of propyl chain remained unchanged for the RR diastereomer (Figure 8B). In the case of the RS diastereomer, the location of the propyl chain initially changed to the nearby hydrophobic region bordered by the B′−C loop and remained unchanged in the unrestrained MD simulation (Figure 8A). The vicinity of the propyl chain to both rings was observed for the RS and RR diastereomer during restrained MD simulations. However, during unrestrained simulation, the propyl chain in the RS diastereomer stabilized closer to the pyridine ring (Figure 8A and Figure S6, Supporting Information), while the propyl chain in the RR diastereomer stabilized closer to the dichlorophenyl ring (Figure 8B and Figure S7, Supporting Information). These results indicate that NOE connectivities of the propyl chain with the pyridine ring are related to the bound state of the RS diastereomer and those with the dichlorophenyl ring to the bound state of the RR diastereomer.

The four possible binding poses of compound **A** (Figures 7 and 8), which are in agreement with the experimental data, indicate that this pyridylethanol(phenylethyl)amine derivative, besides the coordination with the heme iron, interacts with hCYP51 mostly through hydrophobic interactions. The hydrogen bonds between the ligand and protein are not observed. There is a high degree of similarity between the four binding poses. The dichlorophenyl ring is located in the substrate access channel and is firmly positioned between Val130, Tyr131, Leu134, Thr135 (B′ helix), Phe234 (F−F″ loop), His236, Trp239 (F″ helix), Ile379 (K-β1−4 loop), Met381 (β1−4 strand), and Met487 (β4 loop), making numerous contacts with the hydrophobic side chains. In the closest spatial proximity are Tyr131 and Leu134 (B′ helix) (Figures S8−S11, Supporting Information). The chlorine atoms are in the closest spatial proximity to Leu134 (B′ helix), Ile379 (K-β1−4 loop), and Met381 (β1−4 strand) (Figures S8−S11, Supporting Information). The dichlorophenyl ring of compound **A** is positioned deeper in the access channel than the dichlorophenyl ring of econazole (Figure 9B) and also interacts with the hydrophobic residues of the F″ helix, β1−4 strand, and β4 loop as an elongated moiety of ketoconazole (Figure 9A). The pyridine ring is coordinated to the heme iron and is in proximity to the hydrophobic side chains of Ala311, Gly312, Thr315 (I helix), and Ile377 (K-β1−4 loop), like the imidazole ring of ketoconazole and econazole. In contrast to the azoles, the hydrophobic channel near the pyrrole ring D of the heme is not occupied.

The only significant difference between the four binding poses of compound **A** concerns the location of the propyl chain and its orientation with respect to the two aromatic rings. It is located either (i) in the region bordered by helices I and B′ and the F−F″ loop (Figures 7A and B), making hydrophobic contacts with the side chains of Leu310, Ala311 (I helix), and

dx.doi.org/10.1021/ci500556k | J. Chem. Inf. Model. 2014, 54, 3384−3395

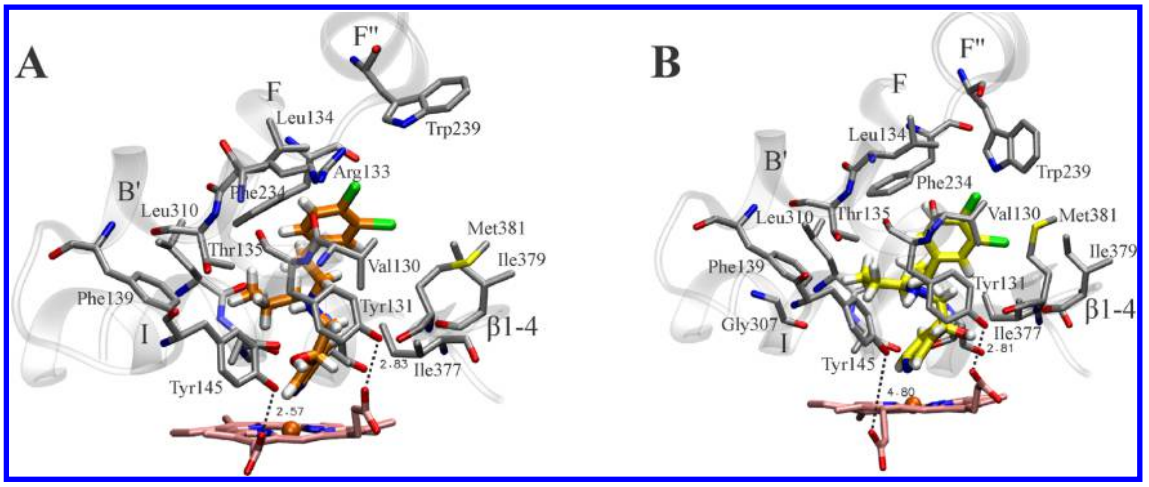

Figure 7. Snapshots from the unrestrained MD trajectories showing the binding poses of the RS (A) and RR (B) diastereomers, with the propyl chain located in the region bordered by helices I and B′ and the F−F″ loop. The amino acids within 4 Å of compound **A** are labeled. The distances between the heme propionates and the side chain oxygens of Tyr131 and Tyr145 are given. The stability of these distances during the unrestrained MD simulations is presented in Figures S16 and S17 of the Supporting Information.

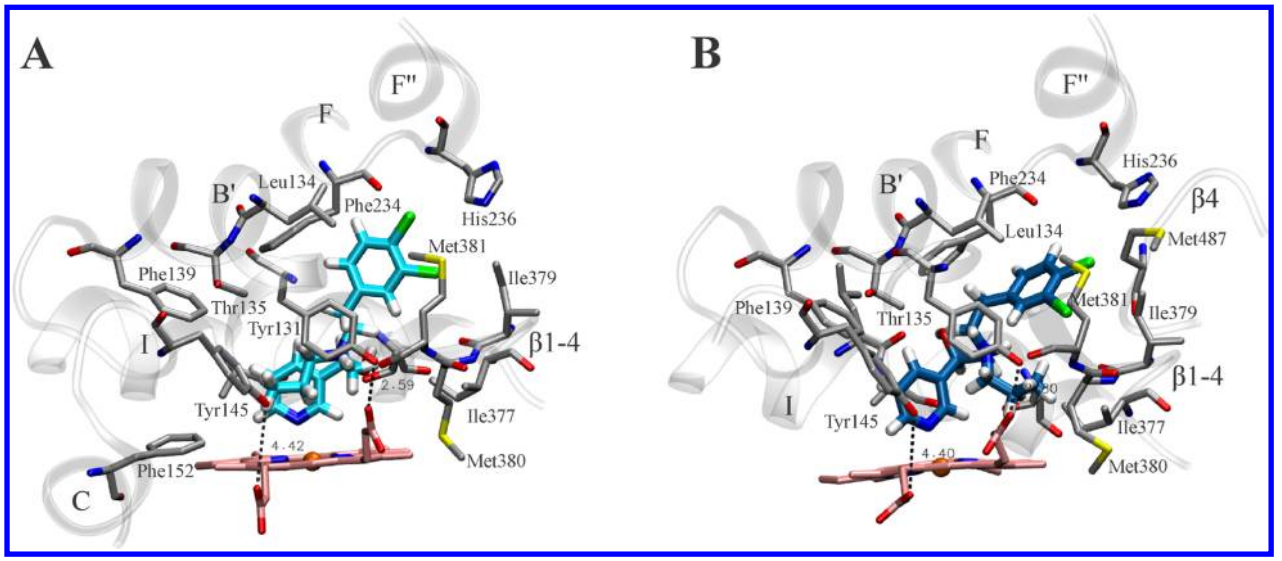

Figure 8. Snapshots from the unrestrained MD trajectories showing the binding poses of the RS diastereomer, with the propyl chain located in the region bordered by the B′−C loop (A), and the RR diastereomer, with the propyl chain located in the region bordered by the β1−4 strand (B). The amino acids within 4 Å of compound **A** are labeled. The distances between the heme propionates and the side chain oxygens of Tyr131 and Tyr145 are given. The stability of these distances during the unrestrained MD simulations is presented in Figures S18 and S19 of the Supporting Information.

Phe234 (F−F″ loop), or (ii) in the region bordered by the B′−C loop (Figure 8A) close to Tyr145 (B′−C loop), or (iii) in the region bordered by the β1−4 strand (Figure 8B), making hydrophobic contacts with the side chains of Ile377 (K-β1−4 loop) and Met380 (β1−4 strand). In the RS diastereomer, the propyl chain is close to the pyridine ring for each location (Figures 7A and 8A), while in the RR diastereomer, the propyl chain is close to the dichlorophenyl ring (Figure 8B) or remote from both rings (Figure 7B).

The results of the BAR calculations revealed that both binding poses of RS diastereomer are energetically more favorable than each binding pose of RR diastereomer, and the most energetically favorable one is the binding pose of the RS diastereomer with the propyl chain located in the region bordered by the B′−C loop (Figure 8A). The alchemical free energy differences between the binding pose of RR diastereomer presented in Figure 7B and the binding poses of RS diastereomer presented in Figures 7A and 8A are −2.71 ± 0.72 and −4.22 ± 0.27 kcal/mol, respectively. The alchemical free energy differences between the binding pose of the RR diastereomer presented in Figure 8B and the binding poses of RS diastereomer presented in Figures 7A and 8A are −2.26 ± 1.43 and −3.48 ± 0.83 kcal/mol, respectively. On the basis of these results, we can conclude that the binding pose of the RS diastereomer presented in Figure 8A is energetically more stable by 1.22 ± 0.59 kcal/mol than the binding pose of this diastereomer presented in Figure 7A. Because the simulations were not long enough to sample the phase space more complete, the error bars cannot be expected to be lower than about ±1 kcal/mol. This is considered very low precision; however, our aim here was to estimate which binding pose is the most stable in order to use this information in the future studies of ligand−CYP51 complexes.

dx.doi.org/10.1021/ci500556k | J. Chem. Inf. Model. 2014, 54, 3384−3395

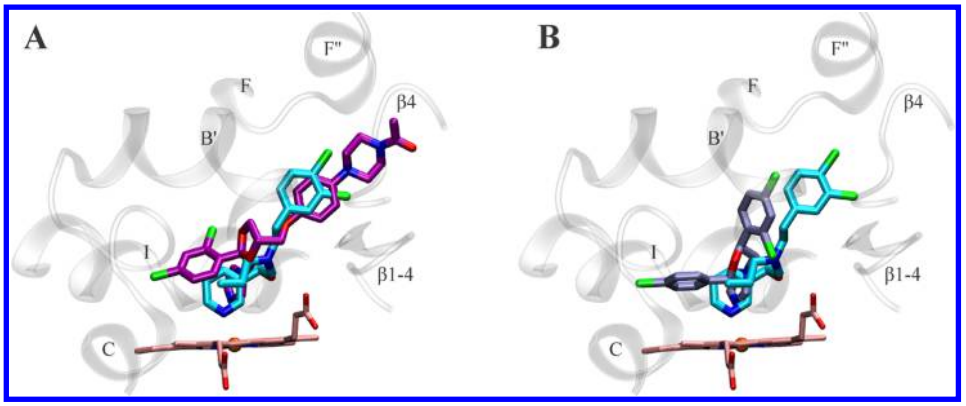

Figure 9. Comparison of the binding mode of compound **A** and azoles to hCYP51. The snapshot is from unrestrained MD trajectories showing the most energetically favorable binding pose of compound **A.** The ketoconazole (A, in purple, crystal structure PDB entry 3LD6)[10] and econazole (B, in ice blue, crystal structure PDB entry 3JUS)[10] are superimposed.

All ligand moieties are firmly positioned in the binding site regions for each binding pose during the unrestrained MD simulations, which are in agreement with the quite uniform STD effects of compound **A** (Figure 5). Slightly stronger STD effects of the dichlorophenyl ring moiety can be explained with its numerous hydrophobic contacts in the substrate access channel. Ligand conformational flexibility is not observed. All the specific orientations of the propyl chain with respect to the aromatic rings are stable, and no pronounced rotations of the two aromatic rings are observed along the MD trajectories (Figures S12−S15, Supporting Information).

Hydrogen-bonding interactions formed by amino acid residues with porphyrin ring propionates are crucial for heme stabilization, for maintaining iron redox potential, and for controlling enzymatic activity.[12,28] The inspection of the hydrogen bonds of porphyrin ring A and D propionates with five amino acid residues, Tyr131, Tyr145, Lys156, Arg382, and His447, during the unrestrained MD simulations, revealed that the hydrogen bond with Tyr145 is broken in most cases (Figures S16−S19, Supporting Information). This hydrogen bond is stable only for the binding pose of the RS diastereomer with the propyl chain positioned in the region bordered by helices I and B′ and the F−F″ loop (Figure 7A). The ability of ligands to disrupt the hydrogen bonds of the heme with corresponding Tyr131 and Tyr145 in the CYP51 orthologs probably plays a role in their high inhibitory potencies and might also be responsible for their selectivity.[6,8,29,30] For the binding pose of the RR diastereomer with the propyl chain positioned in the region bordered by helices I and B′ and the F−F″ loop (Figure 7B), the hydrogen bond of the heme with His447 is also broken. All the other hydrogen bonds of the heme remain stable in each binding pose.

The determination of inhibitors binding mode in human and/or fungal CYP51 is an important step in the development of selective fungal inhibitors and for understanding the structural requirements for selectivity. Mostly due to the lack of more inhibitor-bound CYP51 structures, the structural requirements for selectivity of fungal CYP51 inhibitors are not yet understood. The crystal structures of human CYP51 in complex with ketoconazole and econazole,[10] which are nonselective inhibitors,[10,31,32] do not provide a structural basis for selective inhibition. The binding mode of itraconazole, a selective fungal inhibitor,[31,32] was determined in *S. cerevisiae* CYP51.[5] The authors suggested that the four residues (Leu95, Phe241, His381, and Ser382 *S. cerevisiae* CYP51 numbering; Met100, Trp239, Met378, and Ile379 human CYP51 numbering) that are conserved in fungi but not in human, and are not yet associated with resistance, can provide fungal-specific side-chain contacts for the design of novel selective antifungals. However, the structure itself does not explain the selectivity of the bound inhibitor for fungal CYP51 over the human ortholog. The binding mode of fluconazole, another selective inhibitor,[31,32] has not been determined in fungal or human CYP51. Instead, fluconazole's binding mode was determined in protozoan CYP51s,[7−9] which have low amino acid sequence identity to fungal CYP51s,[33] and some possible explanations for the selectivity of fluconazole and other specific inhibitors for the protozoan CYP51s over human ortholog were proposed. One explanation is based on a unique hydrogen bond network between a specific inhibitor and the protozoan CYP51 (*T. brucei* CYP51) that disrupts the hydrogen bond of Tyr103 (Tyr131 in human CYP51) with the heme propionate, thus altering the heme environment.[6] This specific inhibitor also inhibits *Candida albicans* CYP51 but not human enzyme. The authors suggested that a reason for this inhibitor's selectivity is that the unique hydrogen bond network could not be formed in the human enzyme. Another explanation for selectivity of fluconazole and other specific inhibitors for protozoan CYP51 over human CYP51 is a higher level of flexibility of the human but not protozoan CYP51 enzyme. Human CYP51 has a low energy loop-like region in the middle part of the I helix, which is closest to the heme, whereas in protozoan CYP51s, the I helix is whole. The I helix could hold the heme-coordinated inhibitors within the active site and prevent their replacement by a substrate. This suggests that the relatively weaker susceptibility of human CYP51 to many azole inhibitors can be its intrinsic feature, possibly connected with higher flexibility of the central part of its I helix.[8,33]

The binding mode of the investigated pyridylethanol-(phenylethyl)amine derivative possesses some unique features in comparison to the azoles that can contribute to an understanding of the structural requirements for ligand selectivity. Most importantly, the halogenated phenyl ring, which is the only moiety common to compound **A** and the azoles, is not located in the hydrophobic channel near pyrrole ring D of the heme as in every crystal structure of the azoles in complex with CYP51 orthologs. Instead, it is located in the substrate access channel, where it has a unique set of interactions in comparison to the azoles. Especially, the interactions of the chlorine atoms with unconserved residues

dx.doi.org/10.1021/ci500556k | J. Chem. Inf. Model. 2014, 54, 3384−3395

of the K-β1−4 loop (Ile379) and β1−4 strand (Met381) indicate that modifications of the halogenated phenyl moiety, including its substitution pattern, should be investigated for reduced binding to hCYP51. On the other hand, numerous interactions of compound **A** with conserved residues of the eukaryotic CYP51 active site indicate the potential of these derivatives to inhibit the activity of a fungal CYP51 ortholog. Therefore, we believe that the pyridylethanol(phenylethyl)-amine type of CYP51 inhibitors have a strong potential for the development of selective fungal inhibitors, and we are currently investigating binding of a series of pyridylethanol(phenylethyl)-amine derivatives[15] to fungal and human CYP51.

3. CONCLUSIONS

The binding mode of a pyridylethanol(phenylethyl)amine derivative (**A**), which caused a notable inhibition of cholesterol biosynthesis in a cell assay, to hCYP51 was determined by a combination of spectroscopic and theoretical methods. This is the first determination of the location and interactions of any pyridylethanol(phenylethyl)amine derivative in the CYP51 active site at the atomic level. Unsuccessful attempts to determine the crystal structure of these compounds in complex with CYP51 can be explained by their dynamic nature. The solution-state NMR spectroscopy in combination with the MD simulations used in our studies enabled the investigation of the dynamic and conformational properties of bound ligand **A** in the CYP51 active site.

NMR results indicate that compound **A** binds to hCYP51 in two diastereomeric forms. The application of the spatial relationship between the ligand moieties, defined through the pattern of NOE connectivities, and the spectrophotometrically observed coordination of the ligand pyridine nitrogen to the heme iron in the MD simulations of ligand−hCYP51 complex, enabled the determination of ligand moieties locations in the hCYP51 enzyme active site.

The two diastereomers have a common location of both aromatic ring moieties. The dichlorophenyl ring is firmly positioned in the substrate access channel, making numerous contacts with the hydrophobic side chains. Different locations are observed only for the propyl chain, which is less bulky and can adapt to various hydrophobic regions of the enzyme active site.

The free energy differences between the binding poses of compound **A** obtained by the BAR calculations indicate that the binding of RS diastereomer is energetically more favorable than the RR diastereomer. The most energetically favorable is the binding pose of the RS diastereomer with the propyl chain located in the region bordered by the B′−C loop.

The determination of the CYP51 inhibitor's binding mode to the human CYP51 ortholog is crucial for the development of selective fungal inhibitors. Until now, the binding mode of two azoles to hCYP51 was determined by X-ray crystallography. The binding mode of the investigated pyridylethanol-(phenylethyl)amine derivative possesses some unique features in comparison to the azoles, most importantly, the halogenated phenyl ring, which is the only moiety common to compound **A** and the azoles, is located in the substrate access channel, where it has a unique set of interactions in comparison to azoles. Especially, the interactions with unconserved residues of the K-β1−4 loop (Ile379) and β1−4 strand (Met381) can provide novel directions for the design of selective fungal inhibitors.

4. MATERIALS AND METHODS

4.1. Heterologous Expression in *E. coli* and Isolation of the Recombinant hCYP51 Protein. The pCWOri$^+$/hCYP51 expression plasmid was a generous gift from Dr. Galina I. Lepesheva (Vanderbilt University School of Medicine, Nashville, TN, U.S.A.).[34,35] The first eight amino acid residues of the *hCYP51* construct were modified to MALLLAVF to optimize expression in *E. coli*.[36] The expression construct included the C-terminal histidine tag to facilitate protein purification by Ni^{2+}−nitriloacetic acid (NTA) agarose affinity chromatography. The protein was expressed in the *E. coli* strain HMS174(DE3) (Novagen) and purified using a Ni^{2+}−NTA agarose (Qiagen) column as previously described[28] and carboxymethyl (CM) sepharose, Fast Flow (Sigma), to remove Triton X-100. The protein eluted from Ni^{2+}−NTA agarose was diluted with a C buffer (20 mM potassium phosphate, pH 7.2, 10% glycerol, 0.1 mM EDTA, 0.5 mM PMSF, 10 mM β-mercaptoethanol) and applied to a CM sepharose column equilibrated with a C buffer containing 25 mM NaCl. The column was washed with a C buffer containing 25 mM NaCl and a C buffer containing 100 mM NaCl. The protein was eluted with a C buffer containing 500 mM NaCl. The CYP51 used for NMR studies was then exchanged with a deuterated buffer containing 20 mM Tris-D11, 10% glycerol-D8, 500 mM NaCl in D_2O, and pD 7.2 and was stored at −70 °C until use. The CYP51 used for spectrophotometric titrations was dialyzed against 20 mM Tris-HCl, pH 7.4, 20% glycerol, and 0.1% Triton X-100 and was stored at −70 °C until use. The cytochrome P450 concentration was determined from the absolute absorbance spectra using the extinction coefficient ε_{417} = 117 $mM^{-1}cm^{-1}$. The P450 concentration and the absence of the P420 form were confirmed by reduced CO difference spectra using the extinction coefficient $\varepsilon_{450-490}$ = 91 mM^{-1} cm^{-1}.[37] The molecular weight and purity of the protein was confirmed by SDS-PAGE.

4.2. UV−Visible Spectra and Ligand Binding. Spectra were taken at room temperature using a double beam Shimadzu UV-1800 spectrophotometer. For the ligand binding, 1 μM of hCYP51 in 50 mM phosphate buffer, pH 7.4, 100 mM NaCl, and 10% glycerol was progressively titrated with a ligand until the maximum spectral response was reached. After each incremental addition of the ligand, an equivalent volume of solvent was added to the reference cuvette. Ketoconazole was dissolved in DMSO and compound **A** in water. Spectra were recorded from 350 to 500 nm, and ligand-induced spectral changes were monitored as difference type II spectral responses. Each binding assay was repeated three times. Plots of absorbance changes against ligand concentration were constructed, and the apparent dissociation constants (K_D) were determined by nonlinear regression using GraphPad Prism version 5.04 for Windows (GraphPad Software, San Diego CA, U.S.A.) using a rearrangement of the Morrison equation (quadratic equation)[17] for tight-binding inhibitors (K_D similar or lower than the enzyme concentration):

$$\Delta A = \frac{\Delta A\mathrm{max}}{2[E]} \times \{([E] + [L] + K_D) - (([E] + [L] + K_D)^2 - 4[E][L]^{0.5}\}$$

where ΔA is the peak to trough absorbance change in the difference spectra, ΔAmax is the maximum absorbance change, $[L]$ and $[E]$ are the concentrations of the ligand and the

dx.doi.org/10.1021/ci500556k | J. Chem. Inf. Model. 2014, 54, 3384−3395

enzyme used for the titration, respectively, and K_D is the dissociation constant for the ligand−enzyme complex.

Compound **A** was provided by Lek Pharmaceuticals, a Sandoz Company; the purity determined by HPLC was ≥95%.[16] Ketoconazole was purchased from Sigma; the purity determined by HPLC was ≥99%.

4.3. NMR Spectroscopy. High-resolution NMR spectra were recorded on a Varian DirectDrive 800 MHz spectrometer at 25 °C. All the data were collected using the pulse sequences provided in the Varian libraries of pulse programs.

Compound **A** for the inversion recovery T_1 experiment was prepared in D_2O at 0.4 mM concentration. The inversion recovery T_1 experiment was performed with an 8445.9 Hz spectral width, 32,768 data points, a relaxation delay of 40 s, and 56 scans. Values of the T_1 relaxation times were determined from 10 spectra recorded with recovery delays ranging from 0.6 to 10 s.

NMR samples for the STD and the transferred NOESY experiments were prepared in a buffer containing 20 mM Tris-D11, 10% glycerol-D8, and 100 mM NaCl in D_2O; pD 7.2. DSS (0.1 mM) was used as an internal standard. All the spectra were recorded at a protein/ligand ratio of 1:100. The protein concentration was 4 μM, and the ligand concentration was 0.4 mM.

The transferred NOESY[20,21] spectrum was acquired with an 8802.8 Hz spectral width, 4096 data points in t_2, 64 scans, 256 complex points in t_1, a mixing time of 200 ms, and a relaxation delay of 1.5 s. The residual water signal was suppressed using excitation sculpting,[38,39] and adiabatic pulses[40] were applied for the suppression of zero quantum artifacts during the mixing time. A $T_{1\rho}$ filter of 30 ms was used to eliminate the background protein resonance. The spectrum was processed and analyzed with the FELIX 2007 software package from Felix NMR, Inc. The spectrum was zero-filled twice and apodized with a squared sine bell function shifted by $\pi/2$ in both dimensions.

The STD ligand epitope mapping experiment[23,24] was performed with an 8802.8 Hz spectral width, 16,384 data points, a saturation time of 300 ms, a relaxation delay of 4.3 s, and 12,000 scans. Selective saturation was achieved by a train of 50 ms long Gauss-shaped pulses separated by 1 ms delay. Water was suppressed via excitation sculpting.[38,39] The on-resonance selective saturation of CYP51 was applied at −0.38 ppm. The off-resonance irradiation was applied at 30 ppm for the reference spectrum. Subtraction of the on- and off-resonance spectra was performed internally via phase cycling. The spectrum was zero-filled twice and apodized by an exponential line-broadening function of 2 Hz.

4.4. Docking Calculations. Compound **A** was docked to the hCYP51 structure 3LD6[10] using Glide (Glide, version 5.7, Schrödinger, LCC, New York, NY, 2011).[25−27] The compound was prepared for docking using LigPrep, and its ionization states were predicted by Ionizer for a pH range of 7.0 ± 2.0. The receptor grid was prepared using Receptor Grid Generation. The grid size of 24 Å was used, and the heme Fe was defined as the metal constraint during the standard precision (SP) docking. Each pose was assessed using the GlideScore scoring function.

4.5. Molecular Dynamics Simulation. The representative binding poses of compound **A** as generated by the docking calculations were chosen as starting structures for molecular dynamics (MD) simulations. All the simulations were performed using the CHARMM program[41] using periodic boundary conditions and Ewald method for electrostatics. The canonical ensemble (NVT) was applied for all the calculations at 300 K. The protein was solvated in an explicit water environment modeled by the TIP 3p water model.[42] The sodium and chloride ions were added to achieve the electroneutrality of the system at a physiological concentration.[43] Force field parameters for the protein were obtained from the CHARMM parameter and topology files (version 36) for proteins.[44,45] The oxidation state of the heme Fe was changed from +2 to +3. The proper connection between the heme Fe and Cys449 S atom was achieved by the correct protonation state of Cys449 and an additional bond. UV−visible spectroscopy indicate that the pyridine N is coordinated to the heme Fe as it is the S atom of Cys449; therefore, an additional bond between the heme Fe and the pyridine N of the compound **A** was added.[46,47] This means that all iron-coordinated bonds were treated in the same way. Force field parameters for compound **A** were obtained from the www.paramchem.org Web server based on the CHARMM General Force Field (CGenFF) parameter and topology files (version 2b8) for drug-like molecules.[48] It was considered that the amine N (pK_a = 7.66)[16] of compound **A** is in a protonated state at a physiological pH (7.0 ± 2.0). In order to study the conformational details of the bound ligand, we improved some of the charges and all the flexible torsional angles, namely, charges for atoms C3, C4, C6′, Cl4, Cl3, OH, N1′, NH, C2′, OH, and NH and the following torsional angles: C3′−C7′−C8′−NH; C7′−C8′−NH−C1″; C8′−NH−C8−C7; C8′−NH−C1″−C2″. The torsional angles were fitted to the MP2/6-31G* fully minimized torsional angle scans using the Gaussian-G09 program.[49] In order to balance the force field for all four angles, they were fitted simultaneously using a small python program based on the NumPy and SciPy libraries.[50] To accelerate the simulations, we used two GPU libraries as implemented in the CHARMM program. Most of the simulations used the OpenMM library.[51] However, OpenMM does not support NOE restraints, in which case the MR3 library interfaced to CHARMM program[52] was used. For the same reasons, the additional bonds with the heme Fe were treated as restraints. Moreover, such additional bond treatment is usually preferred over using constraint via the shake method because it simulates the ionic bonding character. NOE-restrained MD simulations were run for 3 ns followed by unrestrained MD simulations for 20 ns. Unrestrained MD simulations were used for further analysis. A Visual Molecular Dynamics (VMD) program was used for the visualization of MD simulations.[53]

The compound **A** parameter files, CHARMM input scripts, and related fitting programs are available on request.

4.6. Bennett's Acceptance Ratio Method (BAR). To calculate the difference in binding free energy between the RS and RR diastereomers of compound **A**, we applied the BAR method[54] using only the end states because the overlap between the two was above the necessary 1% criteria. In order to calculate the energies for which the BAR method was applied, we used the PERT facility as implemented in the CHARMM program and alchemical creations and deletions of the appropriate OH group on the nonperturbed trajectories, so they represent either lambda 0 or 1 states for both the RR or RS diastereomers. For details on the BAR method usage, see König et al.[55] Trajectories produced by the OpenMM GPU library were unable to achieve the 1% overlap criteria, so we used the more accurate MR3 GPU library in CHARMM to report the final RS/RR binding free energy difference.

■ ASSOCIATED CONTENT

Supporting Information

Table with the ^{1}H chemical shift assignment of compound **A** (Table S1), STD spectrum of compound **A** in the presence of hCYP51 (Figure S1), and analysis of unrestrained MD simulations (Figures S2−S21). This material is available free of charge via the Internet at http://pubs.acs.org.

■ AUTHOR INFORMATION

Corresponding Author

*Telephone: +386 1 4760409. Fax: +386 1 4760300. E-mail: simona.grdadolnik@ki.si.

Funding

This work was supported by the Slovenian Research Agency (Grant P1-0010) and EN-FIST Centre of Excellence.

Notes

The authors declare no competing financial interest.

■ ACKNOWLEDGMENTS

We wish to thank Dr. Galina I. Lepesheva (Vanderbilt University School of Medicine, Nashville, Tennessee, U.S.A.) for the generous gift of plasmid pCWOri$^+$/hCYP51.

■ ABBREVIATIONS

BAR, Bennett's acceptance ratio; CYP, cytochrome P450; CYP51, sterol 14α-demethylase; MD, molecular dynamics; NOE, nuclear Overhauser effect; NOESY, nuclear Overhauser effect spectroscopy; PDB, Protein Data Bank; STD, saturation transfer difference; VMD, Visual Molecular Dynamics

■ REFERENCES

(1) Lepesheva, G. I.; Waterman, M. R. Sterol 14α-demethylase cytochrome P450 (Cyp51), a P450 in all biological kingdoms. *Biochim. Biophys. Acta* **2007**, *1770*, 467−477.

(2) Chen, S. C.; Sorrell, T. C. Antifungal agents. *Med. J. Aust.* **2007**, *187*, 404−409.

(3) Becher, R.; Wirsel, S. G. Fungal cytochrome P450 sterol 14α-demethylase (Cyp51) and azole resistance in plant and human pathogens. *Appl. Microbiol. Biotechnol.* **2012**, *95*, 825−840.

(4) Brown, G. D.; Denning, D. W.; Gow, N. A.; Levitz, S. M.; Netea, M. G.; White, T. C. Hidden killers: Human fungal infections. *Sci. Transl. Med.* **2012**, *4*, 165rv113.

(5) Monk, B. C.; Tomasiak, T. M.; Keniya, M. V.; Huschmann, F. U.; Tyndall, J. D.; O'Connell, J. D., 3rd; Cannon, R. D.; McDonald, J. G.; Rodriguez, A.; Finer-Moore, J. S.; Stroud, R. M. Architecture of a single membrane spanning cytochrome P450 suggests constraints that orient the catalytic domain relative to a bilayer. *Proc. Natl. Acad. Sci. U.S.A.* **2014**, *111*, 3865−3870.

(6) Lepesheva, G. I.; Park, H.-W.; Hargrove, T. Y.; Vanhollebeke, B.; Wawrzak, Z.; Harp, J. M.; Sundaramoorthy, M.; Nes, W. D.; Pays, E.; Chaudhuri, M.; Villalta, F.; Waterman, M. R. Crystal structures of *Trypanosoma brucei* Sterol 14α-demethylase and implications for selective treatment of human infections. *J. Biol. Chem.* **2010**, *285*, 1773−1780.

(7) Chen, C. K.; Leung, S. S.; Guilbert, C.; Jacobson, M. P.; McKerrow, J. H.; Podust, L. M. Structural characterization of Cyp51 from *Trypanosoma cruzi* and *Trypanosoma brucei* bound to the antifungal drugs posaconazole and fluconazole. *PLoS Neglected Trop. Dis.* **2010**, *4*, 0000651.

(8) Lepesheva, G. I.; Hargrove, T. Y.; Anderson, S.; Kleshchenko, Y.; Furtak, V.; Wawrzak, Z.; Villalta, F.; Waterman, M. R. Structural insights into inhibition of sterol 14α-demethylase in the human pathogen *Trypanosoma cruzi*. *J. Biol. Chem.* **2010**, *285*, 25582−25590.

(9) Hargrove, T. Y.; Wawrzak, Z.; Liu, J.; Nes, W. D.; Waterman, M. R.; Lepesheva, G. I. Substrate preferences and catalytic parameters determined by structural characteristics of sterol 14α-demethylase (Cyp51) from *Leishmania infantum*. *J. Biol. Chem.* **2011**, *286*, 26838−26848.

(10) Strushkevich, N.; Usanov, S. A.; Park, H.-W. Structural basis of human Cyp51 inhibition by antifungal azoles. *J. Mol. Biol.* **2010**, *397*, 1067−1078.

(11) Poulos, T. L.; Finzel, B. C.; Howard, A. J. High-resolution crystal structure of cytochrome P450cam. *J. Mol. Biol.* **1987**, *195*, 687−700.

(12) Lepesheva, G. I.; Waterman, M. R. Structural basis for conservation in the Cyp51 family. *Biochim. Biophys. Acta* **2011**, *1814*, 88−93.

(13) Vieira, D. F.; Choi, J. Y.; Roush, W. R.; Podust, L. M. Expanding the binding envelope of Cyp51 inhibitors targeting *Trypanosoma cruzi* with 4-aminopyridyl-based sulfonamide derivatives. *ChemBioChem.* **2014**, *15*, 1111−1120.

(14) Rode, B.; Rozman, D.; Fon Tacer, K.; Kocjan, D. Patent WO 2004/007456 A1.

(15) Korosec, T.; Acimovic, J.; Seliskar, M.; Kocjan, D.; Tacer, K. F.; Rozman, D.; Urleb, U. Novel cholesterol biosynthesis inhibitors targeting human lanosterol 14[alpha]-demethylase (Cyp51). *Bioorg. Med. Chem.* **2008**, *16*, 209−221.

(16) Korosec, T.; Grdadolnik, J.; Urleb, U.; Kocjan, D.; Golic Grdadolnik, S. Synthesis, conformation, and stereodynamics of a salt of 2-{[2-(3,4-dichlorophenyl)- ethyl]propylamino}-1-pyridin-3-ylethanol. *J. Org. Chem.* **2006**, *71*, 792−795.

(17) Warrilow, A. G.; Martel, C. M.; Parker, J. E.; Melo, N.; Lamb, D. C.; Nes, W. D.; Kelly, D. E.; Kelly, S. L. Azole binding properties of *Candida albicans* sterol 14-alpha demethylase (Cacyp51). *Antimicrob. Agents Chemother.* **2010**, *54*, 4235−4245.

(18) Balding, P. R.; Porro, C. S.; McLean, K. J.; Sutcliffe, M. J.; Marechal, J. D.; Munro, A. W.; de Visser, S. P. How do azoles inhibit cytochrome P450 enzymes? A density functional study. *J. Phys. Chem. A* **2008**, *112*, 12911−12918.

(19) Lepesheva, G. I.; Villalta, F.; Waterman, M. R. Targeting *Trypanosoma cruzi* sterol 14α-demethylase (Cyp51). *Adv. Parasitol.* **2011**, *75*, 65−87.

(20) Clore, G. M.; Gronenborn, A. M. Theory and applications of the transferred nuclear Overhauser effect to the study of the conformations of small ligands bound to proteins. *J. Magn. Reson.* **1982**, *48*, 402−417.

(21) Clore, G. M.; Gronenborn, A. M. Theory of the time-dependent transferred nuclear Overhauser effect − Applications to structural-analysis of ligand protein complexes in solution. *J. Magn. Reson.* **1983**, *53*, 423−442.

(22) Mayer, M.; Meyer, B. Characterization of ligand binding by saturation transfer difference NMR spectroscopy. *Angew. Chem., Int. Ed.* **1999**, *38*, 1784−1788.

(23) Mayer, M.; Meyer, B. Group epitope mapping by saturation transfer difference NMR to identify segments of a ligand in direct contact with a protein receptor. *J. Am. Chem. Soc.* **2001**, *123*, 6108−6117.

(24) Yan, J.; Kline, A. D.; Mo, H.; Shapiro, M. J.; Zartler, E. R. The effect of relaxation on the epitope mapping by saturation transfer difference NMR. *J. Magn. Reson.* **2003**, *163*, 270−276.

(25) Friesner, R. A.; Banks, J. L.; Murphy, R. B.; Halgren, T. A.; Klicic, J. J.; Mainz, D. T.; Repasky, M. P.; Knoll, E. H.; Shelley, M.; Perry, J. K.; Shaw, D. E.; Francis, P.; Shenkin, P. S. Glide: A new approach for rapid, accurate docking and scoring. 1. Method and assessment of docking accuracy. *J. Med. Chem.* **2004**, *47*, 1739−1749.

(26) Friesner, R. A.; Murphy, R. B.; Repasky, M. P.; Frye, L. L.; Greenwood, J. R.; Halgren, T. A.; Sanschagrin, P. C.; Mainz, D. T. Extra Precision Glide: Docking and scoring incorporating a model of hydrophobic enclosure for protein−ligand complexes. *J. Med. Chem.* **2006**, *49*, 6177−6196.

(27) Halgren, T. A.; Murphy, R. B.; Friesner, R. A.; Beard, H. S.; Frye, L. L.; Pollard, W. T.; Banks, J. L. Glide: A new approach for rapid, accurate docking and scoring. 2. Enrichment factors in database screening. *J. Med. Chem.* **2004**, *47*, 1750−1759.

(28) Lepesheva, G. I.; Virus, C.; Waterman, M. R. Conservation in the Cyp51 family. Role of the B′ helix/Bc loop and helices F and G in enzymatic function. *Biochemistry* **2003**, *42*, 9091−9101.
(29) Hargrove, T. Y.; Wawrzak, Z.; Alexander, P. W.; Chaplin, J. H.; Keenan, M.; Charman, S. A.; Perez, C. J.; Waterman, M. R.; Chatelain, E.; Lepesheva, G. I. Complexes of *Trypanosoma cruzi* sterol 14α-Demethylase (Cyp51) with two pyridine-based drug candidates for chagas disease: Structural basis for pathogen selectivity. *J. Biol. Chem.* **2013**, *288*, 31602−31615.
(30) Andriani, G.; Amata, E.; Beatty, J.; Clements, Z.; Coffey, B. J.; Courtemanche, G.; Devine, W.; Erath, J.; Juda, C. E.; Wawrzak, Z.; Wood, J. T.; Lepesheva, G. I.; Rodriguez, A.; Pollastri, M. P. Antitrypanosomal lead discovery: Identification of a ligand-efficient inhibitor of *Trypanosoma cruzi* Cyp51 and parasite growth. *J. Med. Chem.* **2013**, *56*, 2556−2567.
(31) Warrilow, A. G.; Parker, J. E.; Kelly, D. E.; Kelly, S. L. Azole affinity of sterol 14α-demethylase (Cyp51) enzymes from *Candida albicans* and *Homo sapiens*. *Antimicrob. Agents Chemother.* **2013**, *57*, 1352−1360.
(32) Trosken, E. R.; Adamska, M.; Arand, M.; Zarn, J. A.; Patten, C.; Volkel, W.; Lutz, W. K. Comparison of lanosterol-14 alpha-demethylase (Cyp51) of human and *Candida albicans* for inhibition by different antifungal azoles. *Toxicology* **2006**, *228*, 24−32.
(33) Lepesheva, G. I.; Waterman, M. R. Sterol 14α-demethylase (Cyp51) as a therapeutic target for human Trypanosomiasis and Leishmaniasis. *Curr. Top. Med. Chem.* **2011**, *11*, 2060−2071.
(34) Stromstedt, M.; Rozman, D.; Waterman, M. R. The ubiquitously expressed human Cyp51 encodes lanosterol 14 alpha-demethylase, a cytochrome P450 whose expression is regulated by oxysterols. *Arch. Biochem. Biophys.* **1996**, *329*, 73−81.
(35) Lepesheva, G. I.; Podust, L. M.; Bellamine, A.; Waterman, M. R. Folding requirements are different between sterol 14α-demethylase (Cyp51) from mycobacterium tuberculosis and human or fungal orthologs. *J. Biol. Chem.* **2001**, *276*, 28413−28420.
(36) Barnes, H. J.; Arlotto, M. P.; Waterman, M. R. Expression and enzymatic activity of recombinant cytochrome P450 17 alpha-hydroxylase in *Escherichia coli*. *Proc. Natl. Acad. Sci. U.S.A.* **1991**, *88*, 5597−5601.
(37) Omura, T.; Sato, R. The carbon monoxide-binding pigment of liver microsomes. II. Solubilization, purification, and properties. *J. Biol. Chem.* **1964**, *239*, 2379−2385.
(38) Dalvit, C. Efficient multiple-solvent suppression for the study of the interactions of organic solvents with biomolecules. *J. Biomol. NMR* **1998**, *11*, 437−444.
(39) Hwang, T. L.; Shaka, A. J. Water suppression that works − Excitation sculpting using arbitrary wave-forms and pulsed-field gradients. *J. Magn. Reson., Ser. A* **1995**, *112*, 275−279.
(40) Thrippleton, M. J.; Keeler, J. Elimination of zero-quantum interference in two-dimensional NMR spectra. *Angew. Chem., Int. Ed.* **2003**, *42*, 3938−3941.
(41) Brooks, B. R.; Brooks, C. L., 3rd; Mackerell, A. D., Jr.; Nilsson, L.; Petrella, R. J.; Roux, B.; Won, Y.; Archontis, G.; Bartels, C.; Boresch, S.; Caflisch, A.; Caves, L.; Cui, Q.; Dinner, A. R.; Feig, M.; Fischer, S.; Gao, J.; Hodoscek, M.; Im, W.; Kuczera, K.; Lazaridis, T.; Ma, J.; Ovchinnikov, V.; Paci, E.; Pastor, R. W.; Post, C. B.; Pu, J. Z.; Schaefer, M.; Tidor, B.; Venable, R. M.; Woodcock, H. L.; Wu, X.; Yang, W.; York, D. M.; Karplus, M. Charmm: The biomolecular simulation program. *J. Comput. Chem.* **2009**, *30*, 1545−1614.
(42) Jorgensen, W. L.; Chandrasekhar, J.; Madura, J. D.; Impey, R. W.; Klein, M. L. Comparison of simple potential functions for simulating liquid water. *J. Chem. Phys.* **1983**, *79*, 926−935.
(43) Beglov, D.; Roux, B. Finite representation of an infinite bulk system: Solvent boundary potential for computer simulations. *J. Chem. Phys.* **1994**, *100*, 9050−9063.
(44) MacKerell, A. D.; Bashford, D.; Bellott, M.; Dunbrack, R. L.; Evanseck, J. D.; Field, M. J.; Fischer, S.; Gao, J.; Guo, H.; Ha, S.; Joseph-McCarthy, D.; Kuchnir, L.; Kuczera, K.; Lau, F. T.; Mattos, C.; Michnick, S.; Ngo, T.; Nguyen, D. T.; Prodhom, B.; Reiher, W. E.; Roux, B.; Schlenkrich, M.; Smith, J. C.; Stote, R.; Straub, J.; Watanabe, M.; Wiorkiewicz-Kuczera, J.; Yin, D.; Karplus, M. All-atom empirical potential for molecular modeling and dynamics studies of proteins. *J. Phys. Chem. B* **1998**, *102*, 3586−3616.
(45) Mackerell, A. D., Jr.; Feig, M.; Brooks, C. L., 3rd Extending the treatment of backbone energetics in protein force fields: Limitations of gas-phase quantum mechanics in reproducing protein conformational distributions in molecular dynamics simulations. *J. Comput. Chem.* **2004**, *25*, 1400−1415.
(46) Sundermann, A.; Reif, M. M.; Hofbauer, S.; Obinger, C.; Oostenbrink, C. Investigation of ion binding in chlorite dismutases by means of molecular dynamics simulations. *Biochemistry* **2014**, *53*, 4869−4879.
(47) Park, H.; Lee, S.; Suh, J. Structural and dynamical basis of broad substrate specificity, catalytic mechanism, and inhibition of cytochrome P450 3a4. *J. Am. Chem. Soc.* **2005**, *127*, 13634−13642.
(48) Vanommeslaeghe, K.; Hatcher, E.; Acharya, C.; Kundu, S.; Zhong, S.; Shim, J.; Darian, E.; Guvench, O.; Lopes, P.; Vorobyov, I.; Mackerell, A. D., Jr. Charmm general force field: A force field for drug-like molecules compatible with the Charmm all-atom additive biological force fields. *J. Comput. Chem.* **2010**, *31*, 671−690.
(49) Frisch, M. J.; Trucks, G. W.; Schlegel, H. B.; Scuseria, G. E.; Robb, M. A.; Cheeseman, J. R.; Scalmani, G.; Barone, V.; Mennucci, B.; Petersson, G. A.; Nakatsuji, H.; Caricato, M.; Li, X.; Hratchian, H. P.; Izmaylov, A. F.; Bloino, J.; Zheng, G.; Sonnenberg, J. L.; Hada, M.; Ehara, M.; Toyota, K.; Fukuda, R.; Hasegawa, J.; Ishida, M.; Nakajima, T.; Honda, Y.; Kitao, O.; Nakai, H.; Vreven, T.; Montgomery, J. A., Jr.; Peralta, P. E.; Ogliaro, F.; Bearpark, M.; Heyd, J. J.; Brothers, E.; Kudin, K. N.; Staroverov, V. N.; Kobayashi, R.; Normand, J.; Raghavachari, K.; Rendell, A.; Burant, J. C.; Iyengar, S. S.; Tomasi, J.; Cossi, M.; Rega, N.; Millam, N. J.; Klene, M.; Knox, J. E.; Cross, J. B.; Bakken, V.; Adamo, C.; Jaramillo, J.; Gomperts, R.; Stratmann, R. E.; Yazyev, O.; Austin, A. J.; Cammi, R.; Pomelli, C.; Ochterski, J. W.; Martin, R. L.; Morokuma, K.; Zakrzewski, V. G.; Voth, G. A.; Salvador, P.; Dannenberg, J. J.; Dapprich, S.; Daniels, A. D.; Farkas, Ö.; Ortiz, J. V.; Cioslowski, J.; Fox, D. J. *Gaussian 09*, revision A.08 ; Gaussian, Inc.: Wallingford, CT, 2009.
(50) Oliphant, T. E. Python for scientific computing. *Comput. Sci. Eng.* **2007**, *9*, 10−20.
(51) Eastman, P.; Friedrichs, M. S.; Chodera, J. D.; Radmer, R. J.; Bruns, C. M.; Ku, J. P.; Beauchamp, K. A.; Lane, T. J.; Wang, L.-P.; Shukla, D.; Tye, T.; Houston, M.; Stich, T.; Klein, C.; Shirts, M. R.; Pande, V. S. Openmm 4: A reusable, extensible, hardware independent library for high performance molecular simulation. *J. Chem. Theory Comput.* **2013**, *9*, 461−469.
(52) Narumi, T.; Susukita, R.; Ebisuzaki, T.; McNiven, G.; Elmegreen, B. Molecular dynamics machine: Special-purpose computer for molecular dynamics simulations. *Mol. Simul.* **1999**, *21*, 401−415.
(53) Humphrey, W.; Dalke, A.; Schulten, K. VMD: Visual Molecular Dynamics. *J. Mol. Graph.* **1996**, *14*, 33−38.
(54) Bennett, C. H. Efficient estimation of free energy differences from Monte Carlo data. *J. Comput. Phys.* **1976**, *22*, 245−268.
(55) Konig, G.; Bruckner, S.; Boresch, S. Unorthodox uses of Bennett's acceptance ratio method. *J. Comput. Chem.* **2009**, *30*, 1712−1718.